*applied sciences*

MDPI

*Article*

# Robust Bi-Objective Optimization and Dynamic Modeling of Hydropneumatic Suspension Unit Considering Real Gas Effects

**Di Sun [1], Moonsuk Chang [2] and Jinho Kim [1,*]**

[1] Department of Mechanical Engineering, Yeungnam University, 280 Daehak-Ro, Gyeongsan 712-749, Gyeongbuk-do, Republic of Korea
[2] Dong Won Precision Co., Ltd., Changwon-si 137-717, Gyeongsangnam-do, Republic of Korea
* Correspondence: jinho@ynu.ac.kr

**Abstract:** Vehicles are now rapidly transitioning from a conventional torsion bar suspension to an in-arm suspension unit (ISU), reflecting the growing industrial demand for more compact, high-performance systems. Although the ISU system can adapt well to rough terrain, the side forces produced when the piston moves can affect its reliability. Current models built on ideal gas assumptions fail to describe the complex nonlinear behavior of nitrogen under extreme pressure and temperature variations. This study incorporates the Beattie–Bridgeman real-gas equation into a dynamic force-displacement model to overcome this limitation. Furthermore, a bi-objective optimization strategy was devised that simultaneously minimizes the side forces and enhances acceleration stability across diverse environmental conditions. The optimized design based on a metamodel and a hybrid metaheuristic algorithm resulted in an 81.4% reduction in peak lateral forces and a 53.3% improvement in acceleration robustness, which marks a significant increase in suspension system durability. These findings not only advance ISU design methodologies but also offer viable solutions to existing reliability challenges.

**Keywords:** in-arm suspension unit; robust multi-objective optimization; hydropneumatic suspension; nonlinear damper; metamodeling; hybrid metaheuristic algorithm

check for updates

Received: 16 May 2025
Revised: 9 June 2025
Accepted: 11 June 2025
Published: 17 June 2025

**Citation:** Sun, D.; Chang, M.; Kim, J. Robust Bi-Objective Optimization and Dynamic Modeling of Hydropneumatic Suspension Unit Considering Real Gas Effects. *Appl. Sci.* **2025**, *15*, 6789. https://doi.org/10.3390/app15126789

**Copyright:** © 2025 by the authors. Licensee MDPI, Basel, Switzerland. This article is an open access article distributed under the terms and conditions of the Creative Commons Attribution (CC BY) license (https://creativecommons.org/licenses/by/4.0/).

## 1. Introduction

Tracked vehicles have long been regarded as the optimal solution for traversing irregular and high-dynamic terrains. Their ability to maintain mobility and traction under extreme off-road conditions makes them indispensable in military, agricultural, and exploration applications [1]. Traditionally, torsion bar suspension systems have been widely adopted in such platforms due to their structural simplicity and durability. However, these systems present several limitations, including large installation volume, fixed stiffness, and poor adaptability to variable terrains.

To address these shortcomings, hydropneumatic suspension units (HSUs) have been introduced as compact and modular alternatives. HSUs offer excellent nonlinear stiffness characteristics, high load-bearing capacity, and strong terrain adaptability, with the potential for rapid-response semi-active control [2–4].

Due to the superior performance of HSUs, such systems have received widespread attention in both research and industrial fields. For instance, Els and Van Niekerk developed a dynamic model of a semi-active hydropneumatic spring-damper system for off-road vehicles and highlighted its effectiveness in improving vertical acceleration and ride comfort under rough terrain conditions [5]. Cho and Lee conducted nonlinear modeling of an in-arm hydropneumatic suspension (ISU) system for tracked vehicles, investigating the effects

of orifice diameter and spring preload on vertical dynamic response. Their results demonstrated that structural tuning could effectively yield desirable support characteristics [6]. Qin et al. designed and validated a multi-cylinder hydropneumatic suspension system for a novel road–rail vehicle. They proposed a nonlinear model using AMESim and evaluated various parameters through virtual tests, showing that a hydropneumatic suspension significantly improves adaptability to complex terrain and dynamic performance [7]. Additionally, Nie et al. developed an integrated ISD (Inerter-Spring-Damper) hydropneumatic suspension system for heavy multi-axle vehicles, and experimental validation confirmed its advantages in vibration reduction and impact mitigation [8].

Depending on their structural integration, HSU can be categorized into an in-arm suspension unit (ISU) and on-arm suspension unit (OSU), with ISU offering enhanced compactness and integration capabilities. A key challenge in designing ISU systems is minimizing the side force exerted by the piston on the cylinder wall during its vertical motion. This side force can affect the durability, reliability, and efficiency of the suspension system.

Recently, several cutting-edge works have extended the field of suspension system design. For instance, Viadero-Monasterio et al. [9] developed a robust static output feedback controller for MR-damper-based semi-active suspensions, achieving improved performance under uncertain conditions. In the context of tracked vehicles, nonlinear modeling of MR suspensions has also been explored to enhance dynamic response prediction accuracy [10]. Furthermore, fractional-order SH-GH control strategies have been introduced to ISD-type suspensions for broadband vibration optimization [11]. These approaches represent significant progress toward adaptable and intelligent suspension systems.

However, most of these studies still rely on idealized working media or primarily focus on active control strategies. In industrial applications, the ideal gas (IG) equation or IG-based models are commonly adopted to describe the nonlinear behavior of gas within HSU structures due to their mathematical simplicity. Nevertheless, such simplified approaches fail to accurately capture the temperature-dependent behavior and hysteresis characteristics of real gases [12–14].

This study proposes a systematic model and design framework that integrates real gas thermodynamics and robust optimization strategies to overcome the above limitations. This method particularly adopts the Beattie–Bridgeman real gas equation of state to describe the pressure response behavior of nitrogen under various temperature conditions more accurately [12,15]. Additionally, a bi-objective robust optimization approach was adopted to minimize the side forces and maximize the acceleration robustness (i.e., minimizing the performance sensitivity of acceleration to temperature–frequency variations). Metamodels were constructed to reduce the computational cost, and optimization was performed using a hybrid metaheuristic algorithm.

This study provides a theoretical basis for improving the ISU design by combining real gas modeling and optimization techniques, thereby effectively enhancing the durability and stability of the ISU system.

## 2. Mechanical Modeling of the ISU System

### *2.1. System Overview and Working Principle*

The ISU system integrates the primary suspension components—the spring (elastic element) and damper (damping element)—within the arm structure. The ISU system comprises a main piston, a connecting rod, a compression piston, and a high-pressure nitrogen gas chamber, as shown in Figure 1. As the piston rod moves, the main piston compresses the nitrogen gas, generating spring forces through gas compression and expansion. The hydraulic fluid and lubricant within the cylinder form the damping system, dissipating energy through controlled fluid flow.

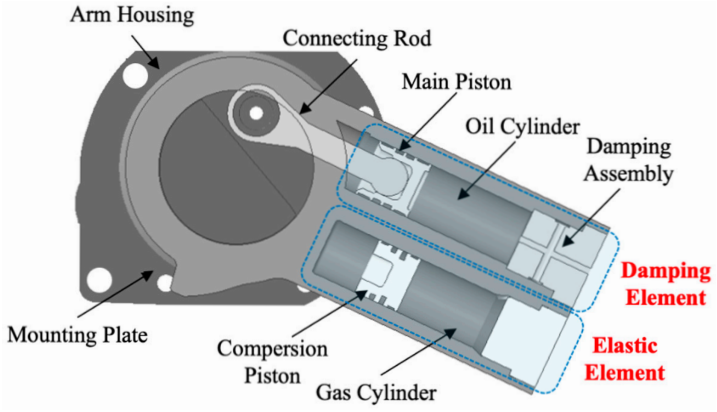



**Figure 1.** The assembled configuration of a typical ISU system.

In this system, the connecting rod connects the suspension support at one end and the main piston on the other via a joint, thereby allowing multi-axis motion. A crank mechanism translates vertical wheel displacement from the load wheel into piston motion, compressing the gas to provide the suspension functionality.

The initial values and physical parameters used in the modeling and simulation of the ISU system are listed in Appendix A. These parameters include geometric dimensions, thermodynamic constants, and damping characteristics, which served as baseline inputs for the numerical analysis.

### *2.2. Kinematic Analysis*

#### 2.2.1. Crank-Housing Angle Calculation

The key structural components of a typical ISU system, along with the coordinate system setup for mechanical design and dynamic analysis, are illustrated in Figure 2. Unlike the OSU system, the ISU housing itself functions as an arm. This implies that the housing undergoes rotational motion in response to the movement of the wheel. A local coordinate system was introduced to accurately describe the kinematic motion characteristics of the ISU, particularly to decouple the mechanical motion from the rotational movement of the arm.

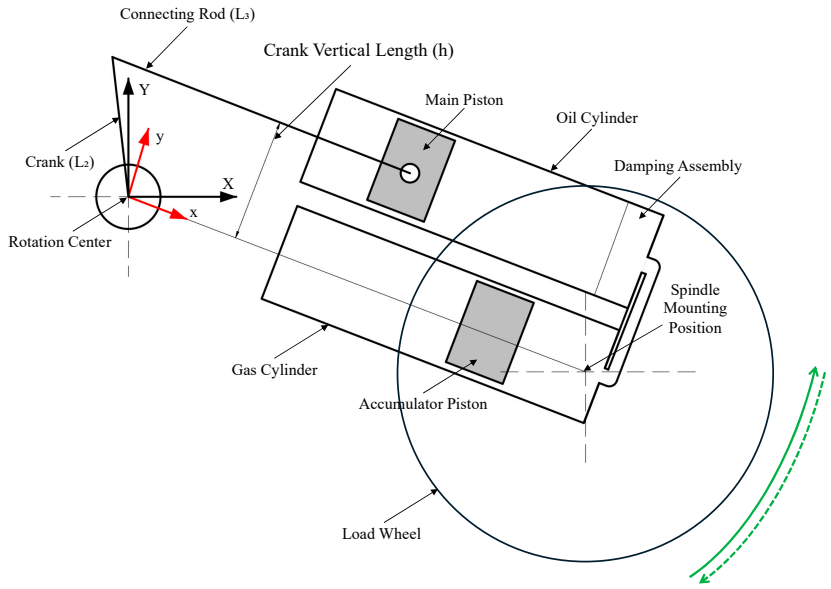
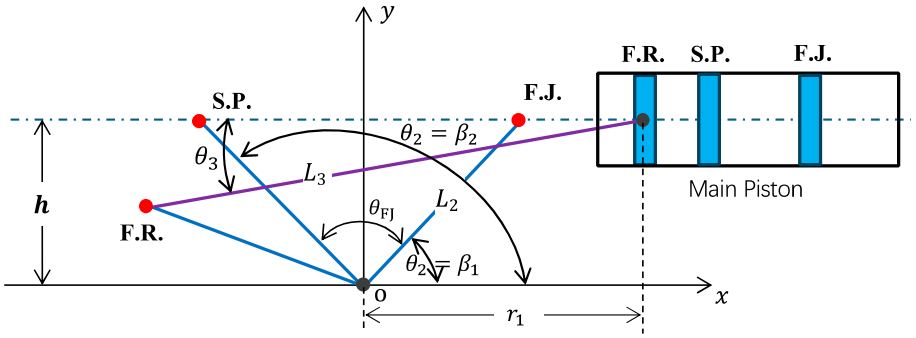



**Figure 2.** Structural components and global-local coordinate systems of a typical ISU system used in kinematic modeling.

In Figure 3, the global coordinate system is represented using the X-Y coordinate system, where the origin is set at the rotation center of the ISU and the x-axis is parallel to the horizontal direction. The global coordinate system remains fixed and is independent of the movement of the robotic arm. The X-Y coordinate system is defined as the local coordinate system, which has the same origin as the global coordinate system. However, the x-axis is parallel to the installation direction of the ISU, and the local coordinate system rotates along with the movement of the robotic arm.




- F.R. (Full Rebound): Maximum extension position
- S.P. (Static Position): Equilibrium position
- F.J. (Full Jounce): Maximum compression position

**Figure 3.** Relationship between crank and main piston motions within the local coordinate system.

By introducing the local coordinate system, the kinematic relationship between the crank and the main piston can be described independently of the rotation of the arm, as shown in Figure 3. The connecting rod aligned with the central axis of the main cylinder in both the static and the full jounce (F.J.) positions, as illustrated in the figure. This configuration was designed to ensure that the side force is reduced to zero both in the initial mounted state of the ISU system and when the nitrogen gas pressure reaches its maximum value at F.J. Therefore, the crank length $L_2$ and the cylinder installation distance $h$ can be calculated using the moment equilibrium equation about the rotational center of the arm in the static position.

$$h = L_2 \cos \frac{1}{2}\theta_{FJ} \tag{1}$$

The wheel position can be expressed as the distance $x$ from the wheel to the horizontal reference line, as shown in Figure 4. The parameters $x$ and $w$ are defined as reference values indicating the position of the wheel. Specifically, $x$ denotes the wheel position measured relative to the horizontal reference, while $w$ represents the wheel position measured relative to the static position. The horizontal reference position was set as $x_{\text{static}} = -0.1630$ m in the static state, whereas the static reference position was defined as $w_{static} = 0$. The relationship between $x$ and w can be described by the following equation.

$$x = w - x_{\text{static}} \tag{2}$$

The angle $\theta_2$ denotes the angle between the crank and the housing. It corresponds to the angle between the $x$-axis of the local coordinate system and $L_1$ and the angle between $L_1$ and $L_2$ in Figures 3 and 4, respectively.

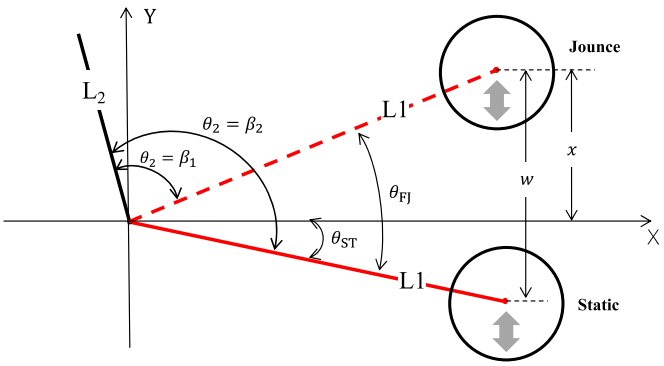



**Figure 4.** Analysis of the wheel position and motion.

The value of $\theta_2$ varied with the wheel movement. Two new variables, $\beta_1$ and $\beta_2$, were introduced to facilitate the calculation of $\theta_2$. The value of $\theta_2$ corresponded to $\beta_1$ when the wheel reached the jounce position, which can be determined using parameter $h$, as shown in Figure 3.

$$\beta_1 = \theta_2^{FJ} = arcsin\left(\frac{h}{L_2}\right) \tag{3}$$

The value of $\theta_2$ corresponded to $\beta_2$ when the wheel was in the static position, and the following expression for $\theta_2$ can be derived from Figure 4.

$$\beta_2 = \theta_2^{ST} = \beta_1 + \theta_{\mathrm{FJ}} \tag{4}$$

From Figure 4, the equation for calculating $\theta_2$ can be formulated as:

$$\theta_2 = \beta_2 - (-\theta_{\mathrm{ST}}) - arcsin\left(\frac{x}{L_1}\right) \tag{5}$$

where $\theta_{ST}$ represents the angle between the arm ($L_1$) and the horizontal reference line in the static state, while $\beta_2 - (-\theta_{ST})$ denotes the value of $\theta_2$ when the wheel is in the horizontal position. The final equation for $\theta_2$ was obtained by combining Equations (2)–(4).

### 2.2.2. Piston Position Derivation

The diagram in Figure 5 is a vectorized, simplified version of Figure 3, represented schematically for computational convenience. This diagram simplifies the geometric relationships between each component using vectors.

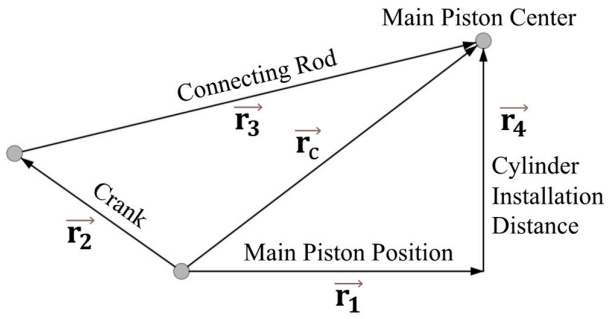



**Figure 5.** Kinematic relationship of the crank-connecting rod–piston system using vectors.

The following expression can be obtained from Figure 5.

$$\boldsymbol{r_c} = \boldsymbol{r_1} + \boldsymbol{r_4} = \boldsymbol{r_2} + \boldsymbol{r_3} \tag{6}$$

Here, the vector representations are given as follows:

$$\boldsymbol{r}_1 = r_1\hat{\boldsymbol{i}}$$

$$\boldsymbol{r}_2 = L_2\left(\cos\ \theta_2\hat{\boldsymbol{i}} + \sin\ \theta_2\hat{\boldsymbol{j}}\right)$$

$$\boldsymbol{r}_3 = L_3\left(\cos\ \theta_3\hat{\boldsymbol{i}} + \sin\ \theta_3\hat{\boldsymbol{j}}\right)$$

$$\boldsymbol{r}_4 = h\hat{\boldsymbol{j}}$$

where $\hat{\boldsymbol{i}}$ and $\hat{\boldsymbol{j}}$ are the respective unit vectors along the horizontal and vertical directions, while $\theta_3$ denotes the deviation angle between the connecting rod and the main cylinder, and $r_1$ corresponds to the piston position.

The following equation was obtained by reorganizing these expressions.

$$r_1\hat{\boldsymbol{i}} + h\hat{\boldsymbol{j}} = L_2\left(\cos\theta_2\hat{\boldsymbol{i}} + \sin\theta_2\hat{\boldsymbol{j}}\right) + L_3\left(\cos\theta_3\hat{\boldsymbol{i}} + \sin\theta_3\hat{\boldsymbol{j}}\right) \tag{7}$$

By separately organizing the equations into their $\hat{\boldsymbol{i}}$ and $\hat{\boldsymbol{j}}$ components, the following relationships can be established.

$\hat{\boldsymbol{i}}$-component:

$$r_1 = L_2\cos\theta_2 + L_3\cos\theta_3 \tag{8}$$

$\hat{\boldsymbol{j}}$-component:

$$h = L_2\sin\theta_2 + L_3\sin\theta_3 \tag{9}$$

Since $\theta_3$ is present in both equations, it can be eliminated to derive an equation for $r_1$. The following expression was obtained from the $\hat{\boldsymbol{j}}$-component equation in the vertical direction:

$$L_3\sin\theta_3 = h - L_2\sin\theta_2 \tag{10}$$

The equation can be simplified down to the following expression by dividing both sides by $L_3$:

$$\sin\theta_3 = \frac{h - L_2\sin\theta_2}{L_3} \tag{11}$$

The following relationship can be derived by applying the trigonometric identity $\sin^2\theta + \cos^2\theta = 1$:

$$\cos\theta_3 = \sqrt{1 - \sin^2\theta_3} \tag{12}$$

The following result was obtained by substituting Equation (11) into Equation (12):

$$\cos\theta_3 = \sqrt{1 - \left(\frac{h - L_2\sin\theta_2}{L_3}\right)^2} \tag{13}$$

Substituting Equation (13) into Equation (8) results in a quadratic equation for the horizontal position $r_1$ of the main piston. The following expression gives the solution to this equation:

$$r_1 = L_2\cos\theta_2 + \left[\left(L_2\cos\theta_2\right)^2 - \left(L_2^2 + h^2 - L_3^2 - 2L_2h\sin\theta_2\right)\right]^{1/2} \tag{14}$$

The main piston displacement can be determined by substituting the values obtained from Equations (1) and (5) into Equation (14).

The following result was derived from Equation (8):

$$\cos\theta_3 = \frac{r_1 - L_2\cos\theta_2}{L_3} \tag{15}$$

The following equation was obtained by combining Equations (11) and (15) and utilizing the trigonometric identity $\tan\theta = \frac{\sin\theta}{\cos\theta}$:

$$\tan\theta_3 = \frac{h - L_2\sin\theta_2}{r_1 - L_2\cos\theta_2} \tag{16}$$

Finally, the value of $\theta_3$ was determined by using the arctangent function.

$$\theta_3 = \tan^{-1}\left(\frac{h - L_2\sin\theta_2}{r_1 - L_2\cos\theta_2}\right) \tag{17}$$

Meanwhile, the displacement of the hydraulic cylinder piston was determined using $r_1$ and its static position $r_{1_static}$ based on Figure 3.

$$\Delta Y = r_1 - r_{1_static} \tag{18}$$

2.2.3. Calculation of the Side Force Applied to the Cylinder Wall

The loads acting on each component of the suspension system are illustrated in Figure 6. These loads were induced by the compression and expansion of nitrogen gas due to the wheel movement, as well as the pressure drop that occurs when the hydraulic fluid passes through the damper.

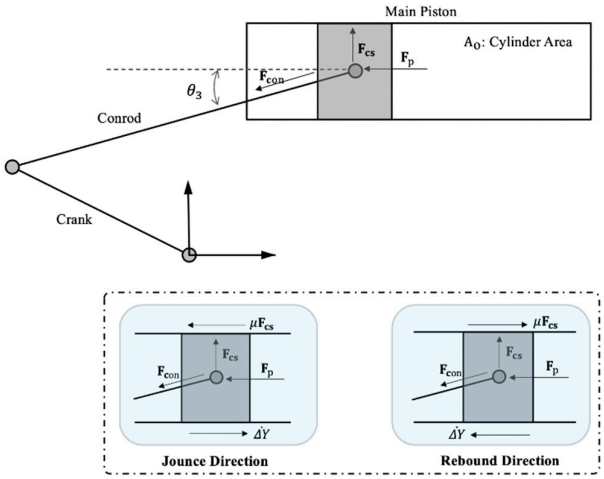



**Figure 6.** Relationships of loads on linkages.

The side force $F_{cs}$ applied to the cylinder wall and the force $F_{con}$ acting on the connecting rod can be expressed as:

$$F_{con} = \frac{F_P - \mu F_{cs}}{\cos(\theta_3)} \tag{19}$$

$$F_{con} = F_{\text{con}}^{PR} + F_{\text{con}}^{c} \tag{20}$$

$$F_{cs} = (F_P - \mu F_{cs})\tan(\theta_3) \tag{21}$$

where $F_P$ represents the parallel force acting on the main piston, $\mu F_{cs}$ denotes the friction force induced by the side force $F_{cs}$, $F_{\text{con}}^{PR}$ corresponds to the force acting on the connecting rod, calculated based on the real gas model, and $F_{\text{con}}^{c}$ represents the damping force acting on the connecting rod.

The friction coefficient $\mu$ between the piston and the cylinder wall was set to zero to simplify the nonlinear force equilibrium analysis.

A system of two nonlinear equations with a single unknown variable was obtained by solving Equations (19) and (20) simultaneously. The solution to this system provided the value of $F_{cs}$.

The connecting rod remained aligned with the central axis of the main cylinder in both the static and the F.J. positions within the local coordinate system, as shown in Figure 3. This structural design ensured that the side force was reduced to zero both in the initial installation state of the ISU system and when the nitrogen gas pressure reached its maximum value at the F.J. position.

To achieve this, the crank length $L_2$ can be determined using the moment equilibrium equation about the rotational center of the arm in the static position, using the following expressions:

$$P_{ni}A_oL_2\cos\frac{1}{2}\theta_{FJ} = m_s\, gL_1\cos\theta_{ST} \tag{22}$$

$$L_2 = \frac{NL_1\cos\theta_{ST}}{P_{ni}A_o\cos\frac{1}{2}\theta_{FJ}} \tag{23}$$

### 2.3. Thermodynamic Modeling of Nitrogen Gas Spring

The selection of nitrogen as the working medium in the HSU system is based on its unique physical and chemical characteristics. Unlike air, nitrogen is chemically inert, avoiding the risk of oxidation to hydraulic fluids and metal components, which is critical for military and off-road vehicles that operate in harsh environments for long periods of time [16].

Recent studies predominantly employ the ideal gas equation of state ($PV = nRT$) to characterize hydropneumatic suspension systems [17–19]. In such models, the pressure–volume relationship of nitrogen gas springs is simplified as $P_N = P_{ni}(\frac{V_{ni}}{V_n})^n$, where the polytropic index $\boldsymbol{n}$ is empirically set to 1.0 for isothermal processes or 1.4 for adiabatic conditions. However, rapid compression cycles can lead to sharp temperature changes in nitrogen within tracked vehicles, which has a significant impact on the dynamic behavior and stiffness characteristics of the hydraulic gas spring, and the calculation of the vehicle dynamic characteristics using the ideal gas model will give a significant error [14].

This study employed the Beattie–Bridgman equation of state to model the real gas behavior of nitrogen, which extends the classical van der Waals model by introducing empirical correction terms for intermolecular forces and volume deviations. Although multiple real gas models with specific applicable ranges are available, previous studies have shown that the Benedict–Webb–Rubin (BWR) equation is particularly well-suited for the typical pressure and temperature conditions of the hydropneumatic suspension systems [20]. The BWR equation can more reliably predict the behavior of nitrogen under dynamic conditions compared to the ideal gas law, and thus improve the calculation accuracy of the dynamic characteristics of the HSP systems during rapid temperature changes [21].

The BWR equation of state is expressed as [22]:

$$P_R = \frac{R(T_0 + 273.15)(1-\epsilon)}{\overline{v}^2}(\overline{v} + B) - \frac{A}{\overline{v}^2} \tag{24}$$

$$\overline{v} = \frac{M\left(V_{ni} - A_g\Delta Z\right)}{m} \tag{25}$$

$$\epsilon = \frac{c}{\overline{v}\ T_0^3} \tag{26}$$

$$A = A_0\left(1 - \frac{a}{\overline{v}}\right) \tag{27}$$

$$B = B_0\left(1 - \frac{b}{\overline{v}}\right) \tag{28}$$

where $P_R$ denotes real gas pressure, $\overline{v}$ represents the molar volume of nitrogen gas, $\epsilon$ corresponds to the temperature correction factor, and $\Delta Z$ is the displacement of the cylinder piston $P_R$.

Assuming that hydraulic oil is incompressible, the displacement of the cylinder piston $\Delta Z$ can be calculated as:

$$\Delta Z = \left(\frac{\mathrm{Ao}}{\mathrm{Ag}}\right)\Delta Y \tag{29}$$

where $\Delta Y$ denotes the displacement of the hydraulic cylinder (main) piston.

Thus, the elastic force $F_k$ and the stiffness load $K_s$ of the hydropneumatic spring can be expressed by the following relationship:

$$F_k = P_R A_O \tag{30}$$

The predicted gas chamber pressures using three thermodynamic models, including isothermal ideal gas ($K$ = 1.0), adiabatic ideal gas ($K$ = 1.4), and Beattie–Bridgeman real gas models, displayed noticeable differences across various vertical wheel displacements, as shown in Figure 7a. These discrepancies amplified significantly as the temperature increased. The predictions from all three models were relatively close within small displacement ranges at an ambient temperature of 20 °C (see Figure 7). However, the differences gradually increased with higher compression levels. Conversely, the deviation between the real gas and the ideal gas models became more pronounced across all displacement ranges, particularly in regions of larger compression when the temperature rose to 120 °C (refer to Figure 7b).

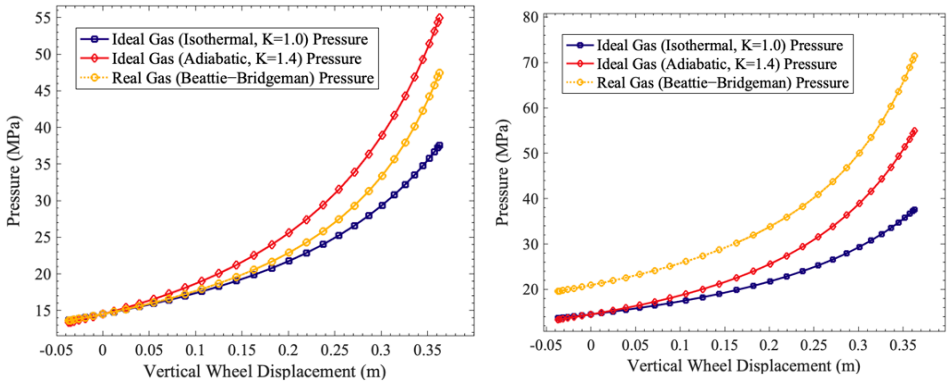



**Figure 7.** Comparison of gas chamber pressure versus vertical wheel displacement under different thermodynamic models (isothermal, adiabatic, and real gas).

The elastic force $F_{wk}$ acting on the wheel can be calculated based on the moment equilibrium principle using the following expression.

$$F_{wk} = \frac{F_{\mathrm{con}}^{PR}\, L_2 \sin\left(\theta_2 - \theta_3\right)}{L_1 \cos\left(\theta_w\right)} \tag{31}$$

The variation in vertical wheel force under real gas assumptions at $T$ = 20 °C and $T$ = 120 °C is presented in Figure 8. It was observed that the suspension system exhibited strong nonlinear behavior, with the force increasing rapidly with displacement. This nonlinear effect was more pronounced at higher temperatures, indicating enhanced suspension stiffness. In particular, the slope of the force–displacement curve became steeper at 120 °C, suggesting increased system rigidity under thermal loading.

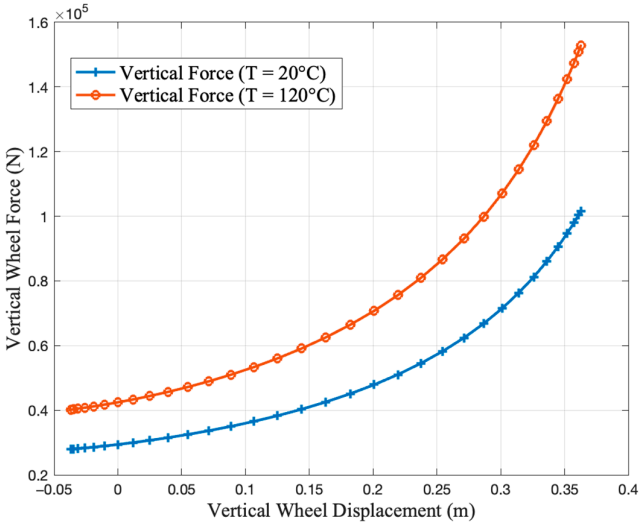



**Figure 8.** Vertical force transmitted to the wheel under real gas assumptions at $T$ = 20 °C and $T$ = 120 °C.

Excessive side forces can lead to increased friction between the piston and the cylinder wall, accelerate component wear, and shorten the service life of the ISU device. In addition, side forces can deform and damage the sealing, resulting in hydraulic oil leakage, which reduces the reliability of the system. Therefore, the size and influence of lateral force must be fully considered in the structural design and parameter optimization of the ISU device to ensure sufficient durability and reliability of the system, especially under large temperature variations.

### *2.4. Damping Characteristics Analysis*

The damping effect primarily originates from the flow resistance exerted by the damping hole and the friction between the piston and the hydraulic cylinder wall. Friction is much smaller compared to the damping force of the damping hole due to the oil lubrication effect, and does not play a major role in damping. Therefore, it can be ignored during the analysis [18].

The direction-dependent damping behavior of the hydraulic circuit was achieved through a combined configuration of damping orifices ($n$) and check valves. Hydraulic oil could flow through the orifice and the open check valve when the wheel moved upward (jounce). This resulted in reduced flow resistance. Conversely, the check valve automatically closed during the downward wheel motion (rebound), forcing all fluid to pass solely through the orifice, producing significantly higher damping forces. This asymmetric damping profile described by the thin-wall orifice throttling theory can be quantified as [23]:

$$F_c = \frac{\rho A_o^3 \dot{\Delta Y}^2 sign\left(\dot{\Delta Y}\right)}{2\left\{nC_z A_z + C_d A_d\left(0.5 + 0.5 sign\left(\dot{\Delta Y}\right)\right)\right\}^2} \tag{32}$$

where $F_c$ denotes the damping force (N), $\dot{\Delta Y}$ represents the piston velocity relative to the cylinder (m/s), while $A_z$ and $A_d$ correspond to the cross-sectional areas of the damping hole and the one-way valve, respectively.

This equation establishes a functional relationship between the damping force and critical parameters, including piston velocity, fluid density, and orifice dimensions. The sign function $sign\left(\dot{\Delta Y}\right)$ encodes motion directionality, outputting +1 during compression and −1 during rebound phases. This formula has been widely referenced in previous studies [19,24,25], underscoring its applicability in various hydropneumatic suspension designs.

The damping force $F_{wc}$ acting on the wheel can be calculated based on the moment equilibrium principle using the following expression.

$$F_{wc} = \frac{F_{\text{con}}^{c} L_2 \sin(\theta_2 - \theta_3)}{L_1 \cos(\theta_w)} \tag{33}$$

For hydraulic damping systems with nonlinear characteristics, the damping coefficient can be represented as a partial derivative of the damping force with respect to the piston velocity.

$$c_s\left(\dot{\Delta Y}\right) = \frac{\partial F_c}{\partial \dot{\Delta Y}} = \frac{\rho A_o^3 \dot{\Delta Y}\, sign\left(\dot{\Delta Y}\right)}{\{nC_z A_z + C_d A_d\left(0.5 + 0.5 sign\left(\dot{\Delta Y}\right)\right)\}^2} \tag{34}$$

## 3. Dynamic Response Analysis of Hydropneumatic Suspension System

### 3.1. Single Degree of Freedom Dynamic Model

The hydropneumatic suspension system was simplified into a one-degree-of-freedom (1-DOF) dynamic model to facilitate analytical modeling and reduce computational complexity, as illustrated in Figure 9. In this model, the suspension is represented by an equivalent spring-damper system connected to a lumped sprung mass $m_s$. The excitation input was given by the vertical road displacement profile $q(t)$, while the response of the sprung mass is denoted by the vertical displacement $x_s$.

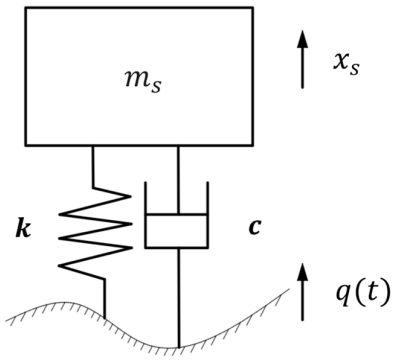



**Figure 9.** Mathematical model for a suspension system with 1-DOF.

This simplification assumes that the tire is completely rigid, i.e., it exhibits no elastic deformation. Consequently, the unsprung mass was neglected, and the suspension system responded directly to the road excitation. This assumption was commonly adopted in heavy tracked vehicle suspension modeling, where the tire compliance was minimal.

The equation of motion governing the vertical dynamics of the sprung mass can be expressed as:

$$m_s \ddot{x}_s = F_{\text{spring}} + F_{\text{damper}} - m_s g \tag{35}$$

where $m_s$ denotes sprung mass, $x_s$ represents sprung mass displacement, and $q$ corresponds to the road profile displacement.

### 3.2. Sinusoidal Displacement Excitation and Acceleration Calculation

A sinusoidal road profile displacement was applied as input to evaluate the dynamic performance of the suspension system:

$$q(t) = A\sin(2\pi f t) \tag{36}$$

where $A$ is the amplitude of the road profile displacement, and $f$ denotes the frequency of the road excitation.

The relationship between the damping force and vertical wheel displacement under sinusoidal excitation with an amplitude of 0.2 m and a frequency of 3 Hz is illustrated in Figure 10. Here, $F_c$ represents the cylinder damping force, while $F_{wc}$ denotes the wheel vertical force (damper). The damping force during the upward motion (compression) was greater than during the downward motion (extension) due to the presence of a one-way valve.

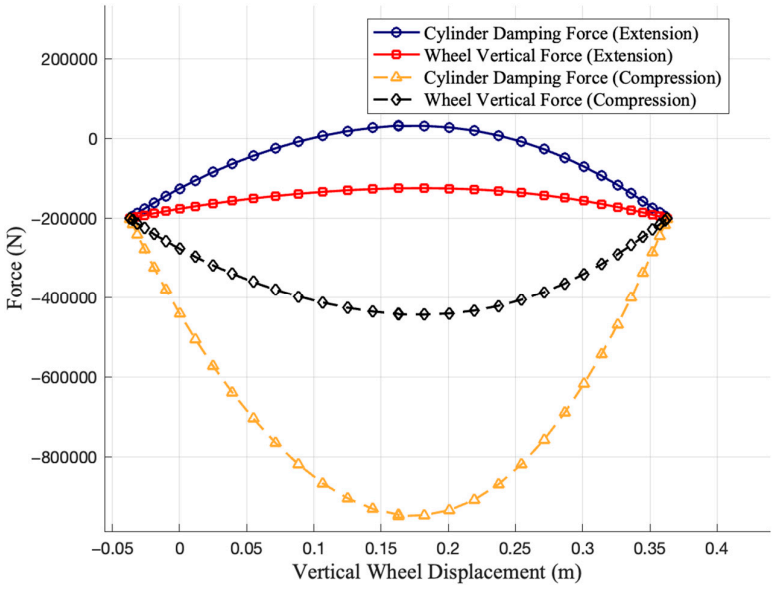



**Figure 10.** Damping force versus vertical wheel displacement under sinusoidal excitation.

As shown in Figure 11, the side force at $T$ = 20 °C and $T$ = 120 °C displayed significant nonlinear characteristics as it varied with the sinusoidal vertical displacement of the wheel. The maximum side force approached 40 kN, posing significant challenges to the cylinder wall and the sealing system.

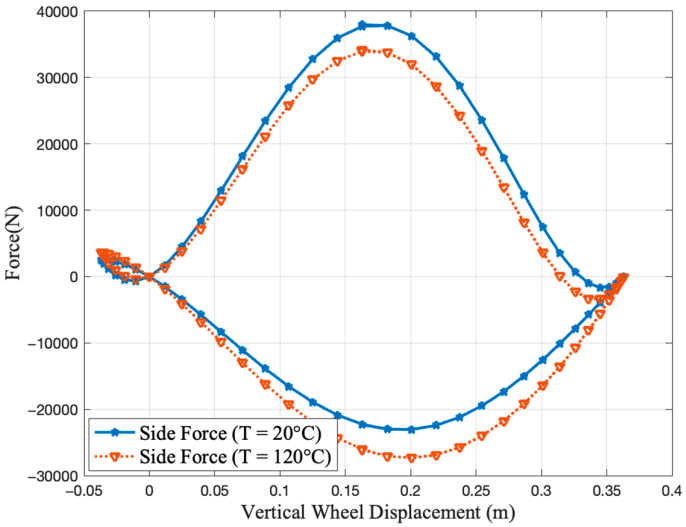



**Figure 11.** Side force on the cylinder wall as a function of the vertical wheel position under real gas conditions at $T$ = 20 °C and $T$ = 120 °C.

### 3.3. Root Mean Square (RMS) Acceleration

The root mean square (RMS) acceleration is an important parameter for assessing the ride comfort because the lower the root mean square value, the better the vibration isolation effect, and the lower the discomfort experienced by the passengers. Therefore, RMS acceleration is the key parameter that needs to be optimized in suspension system designs [26]. By minimizing RMS values, engineers can improve both comfort and dynamic performance under various road conditions, including sinusoidal or random profiles [27].

Mathematically, it can be expressed as:

$$a_{RMS} = \sqrt{\frac{1}{T}\int_0^T \ddot{x}_s^2(t)dt} \tag{37}$$

where $T$ denotes the total evaluation time, and $\ddot{x}_s^2(t)$ represents the instantaneous vertical acceleration of the sprung mass at time $t$. This integral can be approximated using discrete time steps for practical numerical simulations.

The vertical and RMS acceleration of the system were calculated at $T$ = 20 °C and $T$ = 120 °C under sinusoidal excitation with an amplitude of 0.05 m and a frequency of 3 Hz, as shown in Figure 12. The RMS acceleration was calculated to be $RMS = 36.981$ m/s$^2$ at 20 °C (blue line), with the vertical acceleration exhibiting periodic oscillations and peak values reaching approximately $-76$ m/s$^2$. The RMS acceleration increased to $RMS = 38.856$ m/s$^2$ at 120 °C (red line).

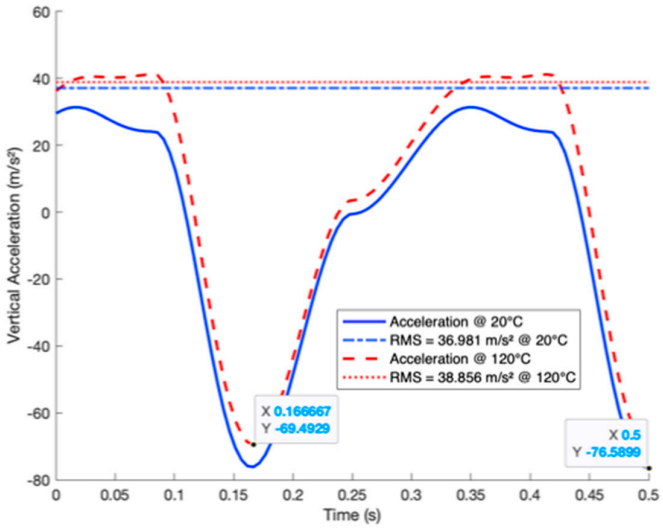



**Figure 12.** Vertical and RMS acceleration under sinusoidal excitation (amplitude = 0.05 m, frequency = 3 Hz).

## 4. Optimization Design

### 4.1. Robust Bi-Objective Optimization Problem Formulation

A bi-objective robust optimization design was performed to further improve the structural safety and environmental adaptability of the ISU system. The optimization simultaneously addressed two critical performance aspects: maximizing acceleration robustness and reducing the peak side force ($F_{cs}$). These objectives are essential for maintaining ride comfort and preventing mechanical failures in varying operational environments.

According to previous studies, the operational temperature of hydropneumatic suspension systems can range from as low as $T = -20$ °C to as high as $T$ = 200 °C under extreme conditions. However, the actual working range generally lies between $T$ = 20 °C and $T$ = 120 °C under typical operating scenarios [28]. Based on this, three representative

temperatures—$T$ = 20 °C, 70 °C, and 120 °C—were selected in this study to assess realistic thermal environments while avoiding extreme edge cases.

The dynamic response of the suspension system was significantly affected by temperature and excitation frequency. The typical travel speed range for vehicles, such as tanks that use ISU suspensions, lies between 10 and 50 km/h. Sinusoidal excitation with frequencies between 1 and 3 Hz can effectively cover most off-road driving scenarios, considering that the typical road impact is between 4 and 6 m. Nine operating conditions were rendered by combining selected temperatures with excitation frequencies of 1, 2, and 3 Hz to evaluate its robustness fully.

The acceleration robustness metric considers both the average and standard deviation of the RMS acceleration under various temperature and frequency conditions, where the mean value ($\mu_{\mathrm{RMS}}$) represents the overall performance level, and the standard deviation ($\sigma_{RMS}$) indicates how much the performance fluctuates with environmental changes. A smaller standard deviation implies higher stability and a more robust system under uncertain conditions.

Excessive side force ($F_{cs}$) presents serious reliability concerns for the ISU system. Accordingly, minimizing the value of $F_{cs}$ is essential to improve durability and operational stability.

Five key design parameters were selected as optimization variables, including crank-arm length ($L_1$), connecting-rod length ($L_3$), orifice diameter ($D_z$), check-valve diameter ($D_d$), and number of damping orifices ($nd$). The RMS acceleration must be lower than 25 m/s$^2$ to ensure passenger comfort, while $L_2$ must be maintained between 0.13 and 0.19 m to meet installation dimensions.

The bi-objective robust optimization problem proposed in this study can mathematically be expressed as follows:

$$\mathit{Design\ Variables}: \ \mathbf{v} = \left[L_1, L_3, D_z, D_d, nd\right]^T$$

$$\mathit{Objective\ Functions}: \begin{cases} \min\limits_{\mathbf{v}} f_1(\mathbf{v}) = \mu_{\mathrm{RMS}}(\mathbf{v}) + \lambda\sigma_{\mathrm{RMS}}(\mathbf{v}), \\ \min\limits_{\mathbf{v}} f_2(\mathbf{v}) = maxF_{\mathrm{side}}(\mathbf{v}). \end{cases}$$

$$\mathit{Constraints}: \begin{cases} a_{\mathrm{RMS}}(\mathbf{v}, T, f) \leq 25\ \mathrm{m/s^2} \\ 0.13\ \mathrm{m} \leq L_2(\mathbf{v}) \leq 0.19\ \mathrm{m} \\ \mathbf{v}_{\min} \leq \mathbf{v} \leq \mathbf{v}_{\max} \end{cases}$$

where the robustness weighting factor $\lambda$ was set equal to 3. Selecting an appropriate robust weighting factor is crucial to balance the mean performance and its variability in robust optimization. Based on previous research and practical experience, the weighting factor $\lambda$ usually ranges between 2 and 5. The weighting factor $\lambda$ = 3 was determined considering the unique operational scenarios of the ISU suspension system as well as the stringent requirements for stability and reliability. This value enhanced the resilience of the system against environmental disturbances without overly conservative trade-offs that would compromise regular operational performance [29].

### 4.2. Optimization Methodology and Experimental Design

The optimization problem proposed in this study was solved using the commercial software PIAnO (Process Integration and Design Optimization, v2025.241015.66, PIDOTECH Inc., Seoul, Republic of Korea), under an academic license. This program has been widely used as it provides design methodology, including designs of experiments, metamodeling, and optimization algorithms [30–32]. A Latin hypercube design (LHD) with 380 sampling

points was implemented to explore the five-dimensional design space spanned by $L_1$, $L_3$, $D_z$, $D_d$, and $n$.

The uniform sampling characteristic of LHD in experimental design can reduce the risk of model overfitting, especially in high-dimensional problems [33–35].

### 4.3. Sensitivity Analysis of Design Variables

As illustrated in Figure 13, the sensitivity analysis quantifies the relative impact of five key design parameters on two performance objectives: the robustness metric of vertical acceleration ($\mu_{\mathrm{RMS}} + 3\sigma_{\mathrm{RMS}}$) and the maximum side force ($F_{cs}$). Among these, the crank-arm length ($L_1$) demonstrated the highest sensitivity in both categories, with indices of 31.8% for acceleration robustness and 43.1% for the side force. The orifice diameter ($D_z$) also exerted significant influence, contributing 25.8% and 13.9% to the two metrics, respectively. Conversely, the check valve diameter ($D_d$) and the connecting rod length ($L_3$) exhibited relatively low sensitivities of 10.7% and 10.4% for robustness, and 1.3% and 30.0% for the side force, respectively. The value of $n$ had a moderate impact, with indices of 21.2% for robustness and 11.7% for the side force.

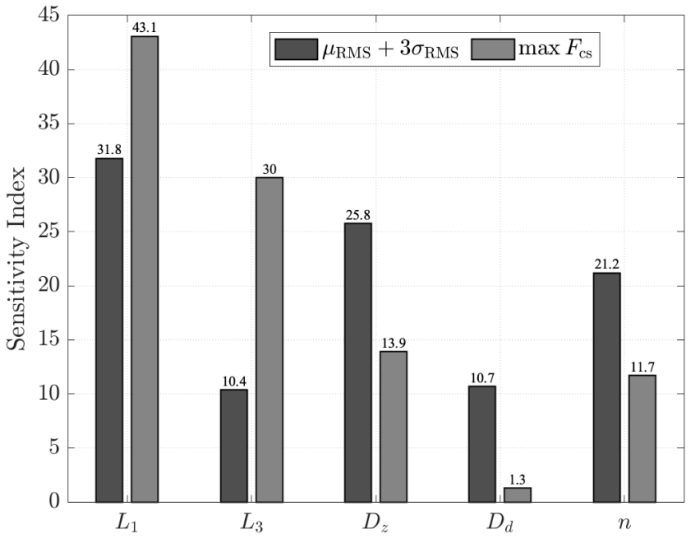
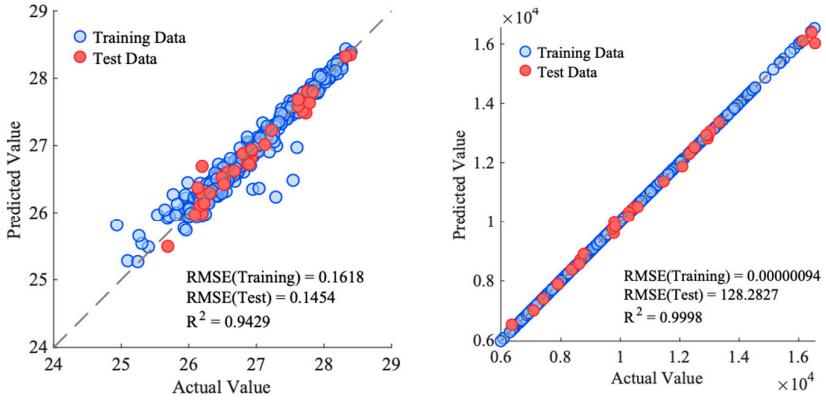



**Figure 13.** Sensitivity analysis.

### 4.4. Metamodel Construction

To improve the optimization efficiency while ensuring high accuracy, 380 sample points were generated in the design space using LHD. A metamodel was developed to approximate the system response based on these samples [36].

The predictive performance of the selected agent model is shown in Figure 14, in which the predicted and actual values of the two objective functions were compared. Among the metamodel candidates—including kriging (KRG), progressive response surface (PRG), and radial basis function (RBF) models—the regularized RBF model offered the best predictive performance for acceleration robustness, achieving a coefficient of determination $R^2 = 0.9429$ and a test RMSE of 0.1454. For the side force objective, the interpolating RBF model yielded excellent accuracy with $R^2 = 0.9998$ and a test RMSE of 128.3 $N$. These results confirmed that the metamodel provided excellent accuracy and can be used for subsequent multi-objective optimization.




(a) $\mu_{\mathrm{RMS}} + 3\sigma_{\mathrm{RMS}}$ *(m/s²)* (b) *max* $F_{cs}$ *(N)*

**Figure 14.** Metamodel prediction performance for the two objective functions: (**a**) acceleration robustness ($\mu_{\mathrm{RMS}} + 3\sigma_{\mathrm{RMS}}$, $\mathrm{m/s^2}$); (**b**) peak lateral force (*max* $F_{cs}$, *N*).

## 5. Results and Discussion

The optimization results are summarized in Tables 1 and 2. The optimal design variables obtained by the hybrid metaheuristic algorithm (HMA) [37] and their comparison with the initial values are provided in Table 2. Significant changes in $D_d$ and $D_z$ values highlight the high sensitivity of these variables to system performance.

**Table 1.** Optimal design variables recommended by HMA compared with the initial values.

| Design Variable | Initial Value | Optimal Value (by HMA) | Change |
|---|---|---|---|
| $L_1$ (m) | 0.4 | 0.5282 | 32.05% |
| $L_3$ (m) | 0.23 | 0.3498 | 52.09% |
| *Dz* (m) | 0.003 | 0.005794 | 93.13% |
| *Dd* (m) | 0.005 | 0.01196 | 139.20% |
| *nd* | 3 | 2 | −33.33% |

**Table 2.** Comparison between predicted and verified optimal objective values.

| Objective | Metamodeler Predicted | Verification | Relative Error (%) |
|---|---|---|---|
| $\mu_{\mathrm{RMS}} + 3\sigma_{\mathrm{RMS}}$ ($\mathrm{m/s^2}$) | 25.46 | 25.50 | 0.17% |
| *max* $F_{cs}$ (N) | 6936.84 | 7096.00 | 2.24% |

A comparison of the predicted values from the metamodels and the actual simulation-based results is provided in Table 2, showing excellent agreement with relative errors below 2.24%. This level of accuracy is within the acceptable range for surrogate-based optimization models and is sufficient to capture global design trends, confirming the accuracy and reliability of the metamodel [38].

For a more intuitive visualization of the optimization effectiveness, Figure 15 provides a comparison between the initial and the optimized objective values for the two objective functions, namely $\mu_{\mathrm{RMS}} + 3\sigma_{\mathrm{RMS}}$ and *max* $F_{cs}$. The logarithmic left y-axis displays the magnitude of objective values, while the right y-axis shows the percentage improvement after optimization.

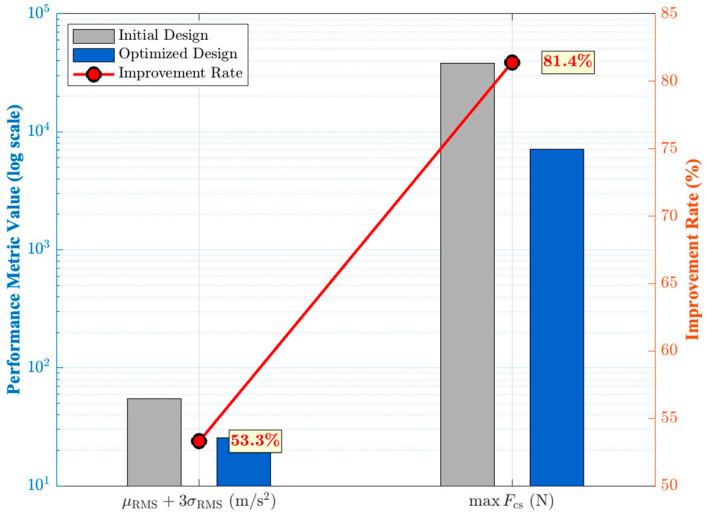



**Figure 15.** Optimization results and improvement percentages for all objectives.

The figure shows that all three objectives experienced substantial reductions after optimization. Specifically, $\mu_{\mathrm{RMS}} + 3\sigma_{\mathrm{RMS}}$ decreased by 53.3%, respectively, reflecting significant improvements in ride comfort and acceleration robustness across different operating conditions. Most notably, the maximum value of $F_{cs}$ reduced by 81.4%, indicating a remarkable reduction in the side force acting on the suspension system. This not only enhanced the structural safety of the system but also minimized potential damage to the internal components due to lateral loads.

Overall, the results confirmed the effectiveness of the HMA-based multi-objective optimization framework, which significantly improved the performance robustness and structural reliability of the ISU suspension system under uncertain operating conditions.

## 6. Conclusions

In this study, a bi-objective robust optimization framework was developed for the ISU hydropneumatic suspension system to enhance acceleration robustness ($\mu_{\mathrm{RMS}} + 3\sigma_{\mathrm{RMS}}$) and reduce the maximum side force ($max\ F_{cs}$). The proposed method effectively addressed system performance uncertainty by considering multiple operating conditions, including varying temperatures and excitation frequencies.

Significant progress was made in both objectives by constructing accurate metamodels and applying HMA. The optimization results demonstrated that the proposed method can satisfy physical constraints while substantially enhancing system stability and ride comfort.

These results suggest that the proposed design methodology is suitable for real-world implementation in tracked military vehicles, off-road exploration platforms, and other mobility systems operating in highly variable and demanding environments. The ISU architecture, with its compact and modular integration of spring and damper elements, provides significant advantages over traditional torsion bar suspensions in terms of spatial efficiency, structural flexibility, and responsiveness to terrain changes.

Future work will focus on integrating semi-active or adaptive control strategies to further improve the dynamic adaptability of ISU under complex excitation inputs. In particular, combining control strategies with temperature feedback can enhance control accuracy and response speed. In this study, traditional optimization techniques, including the construction of surrogate models, were employed to improve optimization efficiency. These approaches could be further enhanced by incorporating machine learning methods, enabling optimal design and analysis with minimal time and resource consumption from experimental design to result evaluation.

Additionally, experimental validation of the proposed real gas model and optimized ISU design will be conducted to bridge the gap between simulation and practical application.

**Author Contributions:** Conceptualization, D.S. and J.K.; Methodology, D.S. and J.K.; Software, D.S.; Validation, D.S. and M.C.; Data curation, M.C.; Writing—original draft, D.S.; Writing—review & editing, M.C. and J.K.; Supervision, M.C. and J.K.; Project administration, J.K. All authors have read and agreed to the published version of the manuscript.

**Funding:** This work was supported by the 2025 Yeungnam University Research Grant.

**Institutional Review Board Statement:** Not applicable.

**Informed Consent Statement:** Not applicable.

**Data Availability Statement:** The original contributions presented in this study are included in the article. Further inquiries can be directed to the corresponding author.

**Conflicts of Interest:** Author Moonsuk Chang was employed by the company Dong Won Precision Co., Ltd. The remaining authors declare that the research was conducted in the absence of any commercial or financial relationships that could be construed as a potential conflict of interest.

## Appendix A. Simulation Parameters

**Table A1.** Input parameters and constants used in the simulation.

| Symbol | Definition | Value | Unit |
|---|---|---|---|
| $L_1$ | Main crank length | $4 \times 10^{-1}$ | m |
| $L_3$ | Connecting rod length | $2.3 \times 10^{-1}$ | m |
| $D_z$ | Damping orifice diameter | $3 \times 10^{-3}$ | m |
| $D_d$ | Check valve diameter | $5 \times 10^{-3}$ | m |
| $n$ | Number of damping orifices | 3 | - |
| $V_{ni}$ | Initial gas volume | $1230 \times 10^{-6}$ | $m^3$ |
| $P_{ni}$ | Initial gas pressure | $145 \times 10^5$ | Pa |
| $T_0$ | Ambient temperatures | [20, 120] | °C |
| $L_{JA}$ | Max jounce displacement | 0.3630 | m |
| $L_{RE}$ | Max rebound displacement | −0.1200 | m |
| $A_o$ | Oil piston area | $6.4 \times 10^{-3}$ | $m^2$ |
| $A_g$ | Gas piston area | $6.4 \times 10^{-3}$ | $m^2$ |
| $x_{static}$ | Vertical offset at static | $-1.63 \times 10^{-1}$ | m |
| $w_{static}$ | Wheel vertical static position | 0 | m |
| $g$ | Gravitational acceleration | 9.8 | $m/s^2$ |
| $N$ | Static vertical load | $2.94 \times 10^4$ | N |
| $\mu$ | Friction coefficient of the cylinder | 0 | - |
| $A_0$ | Real gas coefficient A | $1.362 \times 10^2$ | - |
| $B_0$ | Real gas coefficient B | $5.046 \times 10^{-2}$ | - |
| $a$ | Real gas coefficient a | $2.617 \times 10^{-2}$ | - |
| $b$ | Real gas coefficient b | $-6.91 \times 10^{-3}$ | - |
| $c$ | Real gas coefficient c | $4.2 \times 10^4$ | - |
| $R$ | Universal gas constant | 8.3145 | J/(mol·K) |
| $M$ | Molar mass of nitrogen | 28.013 | kg/kmol |
| $\rho$ | Oil density | 850 | $kg/m^3$ |
| $C_z$ | Damping orifice coefficient | 0.7 | - |
| $C_d$ | Check valve coefficient | 0.6 | - |

## References


1. Wong, J.; Huang, W. "Wheels vs. Tracks"—A Fundamental Evaluation from the Traction Perspective. *J. Terramech.* **2006**, *43*, 27–42. [CrossRef]
2. Dindorf, R. Comprehensive review comparing the development and challenges in the energy performance of pneumatic and hydropneumatic suspension systems. *Energies* **2025**, *18*, 427. [CrossRef]
3. Yang, C.; Gao, X.; Liu, Z.; Cai, L.; Cheng, Q.; Zhang, C. Modeling and analysis of the vibration characteristics of a new type of in-arm hydropneumatic suspension of a tracked vehicle. *J. Vibroeng.* **2016**, *18*, 4627–4646. [CrossRef]
4. Lee, H.; Lee, D. Optimization of maintenance plan for armored vehicle In-armed suspension unit (ISU) based on field data and reliability-centered maintenance. *J. Appl. Reliab.* **2024**, *24*, 75–84. [CrossRef]
5. Els, P.S.; Van Niekerk, J.L. Dynamic Modelling of an Off-Road Vehicle for the Design of a Semi-Active, Hydropneumatic Spring-Damper System. *Veh. Syst. Dyn.* **1999**, *33*, 566–577. [CrossRef]
6. Cho, J.-R.; Lee, H.-W.; Yoo, W.-S.; Lee, J.-K. Study on Damping Characteristics of Hydropneumatic Suspension Unit of Tracked Vehicle. *KSME Int. J.* **2004**, *18*, 262–271. [CrossRef]
7. Qin, B.; Zeng, R.; Li, X.; Yang, J. Design and Performance Analysis of the Hydropneumatic Suspension System for a Novel Road-Rail Vehicle. *Appl. Sci.* **2021**, *11*, 2221. [CrossRef]
8. Nie, J.; Wang, F.; Zhang, X.; Yang, Y. Design and Test of Hydro-Pneumatic ISD Suspension in Heavy Multi-Axle Vehicles. *Adv. Mech. Eng.* **2021**, *13*, 16878140211064737. [CrossRef]
9. Viadero-Monasterio, F.; Meléndez-Useros, M.; Jiménez-Salas, M.; Boada, B.L. Robust Static Output Feedback Control of a Semi-Active Vehicle Suspension Based on Magnetorheological Dampers. *Appl. Sci.* **2024**, *14*, 10336. [CrossRef]
10. Miao, Y.; Rui, X.; Wang, P.; Zhu, H.; Zhang, J.; Wang, J. Nonlinear Dynamic Modeling and Analysis of Magnetorheological Semi-Active Suspension for Tracked Vehicles. *Appl. Math. Modell.* **2024**, *125*, 311–333. [CrossRef]
11. Shen, Y.; Li, J.; Huang, R.; Yang, X.; Chen, J.; Chen, L.; Li, M. Vibration Control of Vehicle ISD Suspension Based on the Fractional-Order SH-GH Stragety. *Mech. Syst. Signal Process.* **2025**, *234*, 112880. [CrossRef]
12. Van Der Westhuizen, S.F.; Els, P.S. Comparison of different gas models to calculate the spring force of a hydropneumatic suspension. *J. Terramech.* **2015**, *57*, 41–59. [CrossRef]
13. Otis, D.R. New Developments in Predicting and Modifying the Performance of Hydraulic Accumulators. *Proc. Natl. Conf. Fluid Power* **1974**, *28*, 473–489.
14. Otis, D.R.; Pourmovahed, A. An Algorithm for Computing Nonflow Gas Processes in Gas Springs and Hydropneumatic Accumulators. *J. Dyn. Syst. Meas. Control.* **1985**, *107*, 93–96. [CrossRef]
15. Kwon, K.; Seo, M.; Kim, H.; Lee, T.H.; Lee, J. Min. Multi-objective optimisation of hydro-pneumatic suspension with gas–oil emulsion for heavy-duty vehicles. *Veh. Syst. Dyn.* **2020**, *58*, 1146–1165. [CrossRef]
16. Liu, Y.; Wang, S.; Li, G.; Mao, B.; Dong, Z.; Li, D. Optimal Parameter Identification of Hydro-Pneumatic Suspension for Mine Cars. *Int. J. Simul. Multidiscip. Des. Optim.* **2024**, *15*, 26. [CrossRef]
17. Solomon, U.; Padmanabhan, C. Hydro-Gas Suspension System for a Tracked Vehicle: Modeling and Analysis. *J. Terramech.* **2011**, *48*, 125–137. [CrossRef]
18. Qiao, C.; Wen, H.; Liu, X.; Wang, G. Damping control and experiment on active hydro-pneumatic suspension of sprayer based on genetic algorithm optimization. *Front. Neurorobot.* **2021**, *15*, 707390. [CrossRef]
19. Yang, F.; Du, Y.; Wen, C.; Li, Z.; Mao, E.; Zhu, Z. Optimization design of the hydro-pneumatic suspension system for high clearance self-propelled sprayer using improved MOPSO algorithm. *Int. J. Agric. Biol. Eng.* **2024**, *17*, 109–122. [CrossRef]
20. Els, P.S.; Theron, N.J.; Uys, P.E.; Thoresson, M.J. The Ride Comfort vs. Handling Compromise for off-Road Vehicles. *J. Terramech.* **2007**, *44*, 303–317. [CrossRef]
21. Beattie, J.A.; Bridgeman, O.C. A new equation of state for fluids. I. Application to gaseous ethyl ether and carbon dioxide1. *J. Am. Chem. Soc.* **1927**, *49*, 1665–1667. [CrossRef]
22. Beattie, J.A.; Bridgeman, O.C. A New Equation of State for Fluids. II. Application to Helium, Neon, Argon, Hydrogen, Nitrogen, Oxygen, Air and Methane. *J. Am. Chem. Soc.* **1928**, *50*, 3133–3138. [CrossRef]
23. Zhu, X.; Guan, J.; Liu, Z.; Li, Y.; Yang, R. Fuzzy PID control of single chamber semi active hydro-pneumatic suspension based on GA optimization. In Proceedings of the 2024 43rd Chinese Control Conference (CCC), Kunming, China, 28–31 July 2024; 2024; pp. 792–797. [CrossRef]
24. Sun, H.; Li, R.; Xu, J.; Xu, F.; Zhang, B.; Dong, X. Fractional modeling and characteristic analysis of hydro-pneumatic suspension for construction vehicles. *Processes* **2021**, *9*, 1414. [CrossRef]
25. Li, Z.; Zhao, S.X.; Sun, B.; Gao, S.; Gao, Y.; Guo, B.; Liu, Z.; Liu, F. Performance and optimization of the hydropneumatic suspension of high-speed wheeled excavators. *Eng. Lett.* **2023**, *31*, 974.
26. Dridi, I.; Hamza, A.; Ben Yahia, N. A New Approach to Controlling an Active Suspension System Based on Reinforcement Learning. *Adv. Mech. Eng.* **2023**, *15*, 1–21. [CrossRef]
27. Yin, Y.; Rakheja, S.; Boileau, P.-E. Multi-performance analyses and design optimisation of hydro-pneumatic suspension system for an articulated frame-steered vehicle. *Veh. Syst. Dyn.* **2019**, *57*, 108–133. [CrossRef]

28. Els, P.S.; Grobbelaar, B. Heat Transfer Effects on Hydropneumatic Suspension Systems. *J. Terramech.* **1999**, *36*, 197–205. [CrossRef]
29. Zhang, L.; Waza Muluken, T.; Dong, E. Robust Optimization Design of Suspension System Based on Spatial Structure. In Proceedings of the 2019 International Conference on Computer Network, Electronic and Automation (ICCNEA), Xi'an, China, 27–29 September 2019; pp. 474–479. [CrossRef]
30. Sun, D.; Park, S.; Wang, S.; Hwang, K.; Song, S.; Choi, W.; Park, J.; Kim, J. Shape optimization for the stability and lightweighting of the upper sliding rail of an automotive monopost seat. *Int. J. Automot. Technol.* **2024**, *25*, 1011–1023. [CrossRef]
31. Lee, J.H. Development of system characteristic optimization method to achieve vehicle target performance. *Int. J. Automot. Technol.* **2024**, *25*, 295–303. [CrossRef]
32. Experimental analysis of vacuum membrane dehumidifier: Hollow fiber module designs and dehumidification performance. *Appl. Therm. Eng.* **2024**, *236*, 121848. [CrossRef]
33. Li, G.; Yang, J.; Wu, Z.; Zhang, W.; Okolo, P.; Zhang, D. A Sequential Optimal Latin Hypercube Design Method Using an Efficient Recursive Permutation Evolution Algorithm. *Eng. Optim.* **2024**, *56*, 179–198. [CrossRef]
34. Katamesh, N.S.; Abbas, A.E.F.; Mahmoud, S.A. Four Chemometric Models Enhanced by Latin Hypercube Sampling Design for Quantification of Anti-COVID Drugs: Sustainability Profiling through Multiple Greenness, Carbon Footprint, Blueness, and Whiteness Metrics. *BMC Chem.* **2024**, *18*, 54. [CrossRef] [PubMed]
35. Xu, Z.; Xia, D.; Yong, N.; Wang, J.; Lin, J.; Wang, F.; Xu, S.; Ge, D. Hybrid Particle Swarm Optimization for High-Dimensional Latin Hypercube Design Problem. *Appl. Sci.* **2023**, *13*, 7066. [CrossRef]
36. Simpson, T.W.; Poplinski, J.D.; Koch, P.N.; Allen, J.K. Metamodels for Computer-Based Engineering Design: Survey and Recommendations. *Eng. Comput.* **2001**, *17*, 129–150. [CrossRef]
37. Park, K.-B. An Efficient Hybrid Metaheuristic Algorithm for Solving Constrained Global Optimization Problems. Ph.D. Thesis, Hanyang University, Seoul, Republic of Korea, February 2016.
38. Yepes-Bellver, L.; Brun-Izquierdo, A.; Alcalá, J.; Yepes, V. Artificial Neural Network and Kriging Surrogate Model for Embodied Energy Optimization of Prestressed Slab Bridges. *Sustainability* **2024**, *16*, 8450. [CrossRef]


**Disclaimer/Publisher's Note:** The statements, opinions and data contained in all publications are solely those of the individual author(s) and contributor(s) and not of MDPI and/or the editor(s). MDPI and/or the editor(s) disclaim responsibility for any injury to people or property resulting from any ideas, methods, instructions or products referred to in the content.